






On the Magnitude of Canyon-Induced Mixing

Robert H. Nazarian¹ , Christian M. Burns^{1,2}, Sonya Legg³ , Maarten C. Buijsman⁴ , Harpreet Kaur⁴ , and Brian K. Arbic⁵ 

¹Fairfield University, Fairfield, CT, USA, ²University of Massachusetts Lowell, Lowell, MA, USA, ³Princeton University, Princeton, NJ, USA, ⁴University of Southern Mississippi, Hattiesburg, MS, USA, ⁵University of Michigan, Ann Arbor, MI, USA

Key Points:

- We present a framework for estimating the range of global internal tide-driven dissipation in submarine canyons
- Submarine canyons may dissipate approximately 5% of the energy input into the global internal tides
- Prior estimates of canyon-driven dissipation may be underestimates, as regions of max canyon-induced mixing have been un- or under-observed

Correspondence to:

R. H. Nazarian,
nazarian@fairfield.edu

Citation:

Nazarian, R. H., Burns, C. M., Legg, S., Buijsman, M. C., Kaur, H., & Arbic, B. K. (2021). On the magnitude of canyon-induced mixing. *Journal of Geophysical Research: Oceans*, 126, e2021JC017671. <https://doi.org/10.1029/2021JC017671>

Received 14 JUN 2021
 Accepted 1 NOV 2021

Abstract The location of mixing due to internal tides is important for both the ocean circulation as well as local biogeochemical processes. Numerous observations and modeling studies have shown that submarine canyons may be regions of enhanced internal tide-driven mixing, but there has not yet been a systematic study of all submarine canyons resolved in bathymetric datasets. Here, we parameterize the internal tide-driven dissipation from a suite of simulations and pair this with a global high-resolution, internal tide-resolving model and bathymetric dataset to estimate the internal-tide-driven dissipation that occurs in all documented submarine canyons. We find that submarine canyons dissipate a significant fraction of the incoming internal tide's energy, which is consistent with observations. When globally integrated, submarine canyons are responsible for dissipating 30.8–75.3 GW, or 3.2%–7.8% of the energy input into the M_2 -frequency internal tides. This percentage of the internal tide energy that is dissipated in submarine canyons is comparable to or larger than previous calculations using extrapolations from observations of single canyons.

Plain Language Summary Internal waves, or waves that propagate in density layers below the surface of the ocean, are responsible for transporting a significant amount of energy throughout the ocean. When these waves break, they deposit their energy in local mixing events. Submarine canyons have been identified as a type of topography that leads to significant internal wave-driven mixing. In this study, we use a global map of canyons, together with a high-resolution ocean model, to calculate the percentage of internal wave energy that is lost to mixing in submarine canyons. We find that a significant fraction of the incident internal wave energy is lost within each submarine canyon. We then sum the energy loss for all submarine canyons to calculate the amount of internal wave-driven mixing that occurs within canyons over the global ocean. We find that approximately 5%, a non-negligible amount, of the energy in the global M_2 -frequency internal wavefield is lost in canyons. This percentage of the internal wave energy that is lost in submarine canyons is comparable to or larger than previous calculations using extrapolations from observations of single canyons.

1. Introduction

1.1. Internal Wave Dynamics

Diapycnal mixing, or mixing across density surfaces, is important in sustaining the large-scale circulation of the ocean (Bryan, 1987; Wunsch & Ferrari, 2004). While there are a host of physical processes through which diapycnal mixing may occur, the breaking of tidally generated internal waves (internal tides) has been shown to be an efficient mechanism for diapycnal mixing in the ocean (Egbert & Ray, 2000; de Lavergne et al., 2019; Munk & Wunsch, 1998; Polzin et al., 1997; Vic et al., 2019; Whalen et al., 2012; Waterhouse et al., 2014; Yi et al., 2017). These waves efficiently transmit energy over ocean basins (Zhao et al., 2016), and deposit this energy to turbulent mixing where they break.

The reflection of internal tides off topography has been identified as a particularly efficient driver of diapycnal mixing (Johnston & Merrifield, 2003; Klymak et al., 2011; Legg, 2014; MacKinnon et al., 2017) and depends on the slope criticality, which we define as

$$s = \frac{|\tan\alpha|}{|\tan\theta_g|} \quad (1)$$

© 2021. The Authors.

This is an open access article under the terms of the [Creative Commons Attribution-NonCommercial-NoDerivs License](https://creativecommons.org/licenses/by-nc-nd/4.0/), which permits use and distribution in any medium, provided the original work is properly cited, the use is non-commercial and no modifications or adaptations are made.

where α is the angle of inclination of the topography and θ_g is the angle of the group velocity vector, both taken relative to the horizontal. Numerous studies have suggested that critical ($s = 1$) and near-critical slopes lead to enhanced levels of dissipation (Cacchione & Wunsch, 1974; Eriksen, 1982).

1.2. Internal Wave-Driven Dissipation in Canyons

Submarine canyons are regions of enhanced levels of internal tide-driven mixing due to both their geometry and their relative abundance, with over 10% of the continental slope intersected by canyons (Alberty et al., 2017; Aslam et al., 2018; Bosley et al., 2004; Bruno et al., 2006; Carter & Gregg, 2002; Codiga et al., 1999; Gardner, 1989; Gordon & Marshall, 1976; Gregg et al., 2011; Hall & Carter, 2011; Hamann et al., 2021; Hotchkiss & Wunsch, 1982; Kunze et al., 2012; Lee et al., 2009; Nazarian & Legg, 2017a, 2017b; Petruncio et al., 1998; Wain et al., 2013; Waterhouse et al., 2017; Xu & Noble, 2009). Diapycnal mixing within canyons is important for a host of coastal processes (Cacchione et al., 2002; Leichter et al., 2003; McPhee-Shaw, 2006; Ramos-Musalem & Allen, 2019), and for the large-scale circulation of the ocean, as mixing at depth sustains the global overturning circulation (Melet et al., 2016; Munk, 1966).

Prior observations and modeling studies have been useful in elucidating the physical processes by which canyon-induced mixing occurs. Hamann et al. (2021) conducted a comparison of data collected at disparate canyons to consider the mechanisms by which enhanced dissipation occurs and, while there is a range of physical processes leading to turbulent dissipation, many of the canyons analyzed share the same reflection and dissipative processes as the modeling studies of Nazarian and Legg (2017a, 2017b); namely reflection leading to (a) scattering to higher modes and (b) wave focusing. These processes are also consistent with additional idealized simulations of internal wave-driven mixing in Eel and Veatch Canyons (Nazarian, 2018) as well as a host of observations (Alberty et al., 2017; Aslam et al., 2018; Bruno et al., 2006; Codiga et al., 1999; Gardner, 1989; Hall & Carter, 2011; Hamann et al., 2021; Hotchkiss & Wunsch, 1982; Kunze et al., 2012; Lee et al., 2009; Petruncio et al., 1998; Wain et al., 2013; Waterhouse et al., 2017). While there are other dissipative processes observed in other canyons, such as a flow reversal in Ascension Canyon (Gregg et al., 2011) or standing wave structure in Eel Canyon (Waterhouse et al., 2017), dissipation due to internal tide scattering to higher modes and increased energy density due to wave reflection and focusing is likewise observed in these cases. Hence, while there are a host of processes by which internal tides may become unstable and break in submarine canyons, reflection processes are one of the main mechanisms by which dissipation occurs, and will be the focus of this study.

While prior studies have been informative regarding the physical processes by which internal tides break and lead to mixing within canyons, they have not provided a robust calculation of the globally-integrated mixing within canyons. Based on observations of Monterey Canyon, it was suggested that approximately 15 GW is dissipated in canyons (Gregg et al., 2005). Conducting such estimates of the global canyon-induced mixing from observations or modeling studies of single canyons is difficult, as canyons have variations in their shape and size, which may modulate their efficiency in inducing local dissipation. Additionally, these calculations do not include information about the magnitude of internal tide energy incident at the canyon. Therefore, a calculation of dissipation within every submarine canyon is necessary to more accurately estimate the global fraction of canyon-driven dissipation due to internal tide reflection processes.

1.3. Canyon Datasets

Such a calculation, however, has not previously been conducted due to the limitations of prior bathymetric datasets. Specifically, Harris and Whiteway (2011) undertook a comprehensive identification (and subsequent analysis of the geometric parameters) of submarine canyons using the ETOPO1 bathymetric data set with a moderate resolution of 1 arc-minute. Based on their analysis, Harris and Whiteway (2011) identified 5,849 separate, large-scale submarine canyons. While this study presented a significant step forward in creating an inventory of the global distribution of canyons, it still lacked the high resolution to identify smaller canyons, and incorrectly identified multiple, nearby canyons as one larger canyon.

A follow-up study by Harris et al. (2014) utilized the Shuttle Radar Topography Mapping (SRTM) 30-arc s database (Becker et al., 2009) to conduct a global inventory of 29 unique geomorphic features, including submarine canyons. With the higher resolution, Harris et al. (2014) were able to identify smaller-to

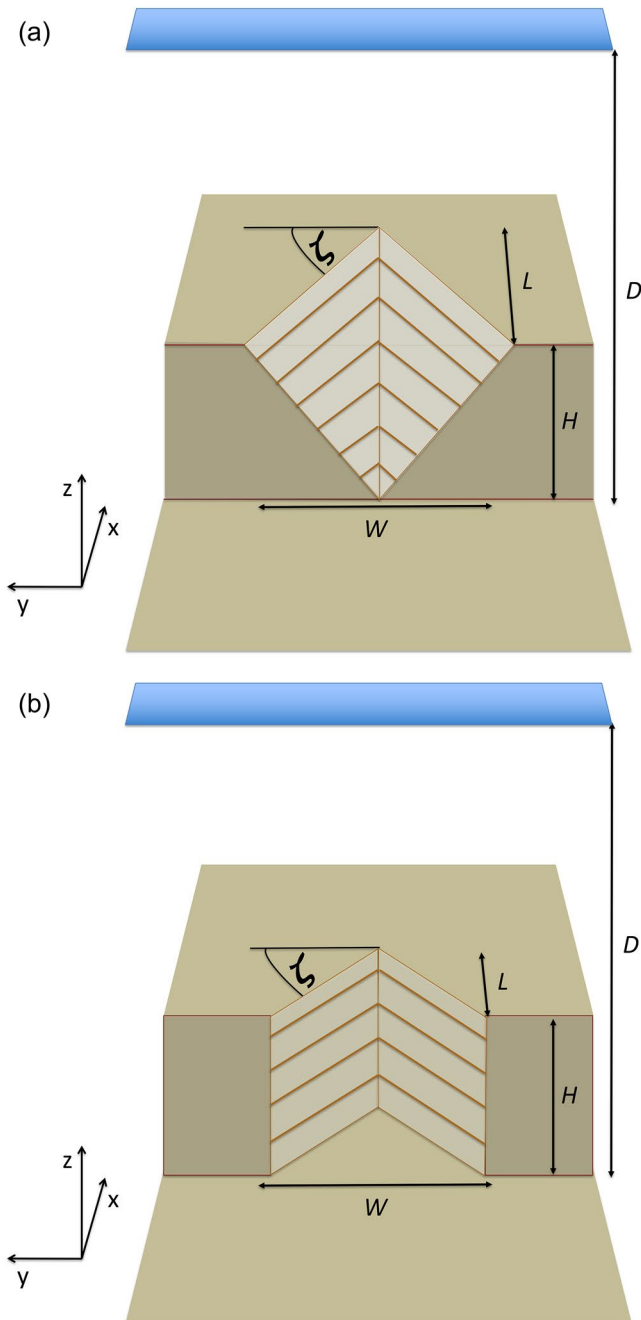


Figure 1. Diagram of canyon topography to illustrate the geometric variables used in the parameterization, including canyon height, H , depth D , width, W , length, L , and aspect ratio, ζ . (a) Near-critical slope and (b) flat bottom canyon topography.

moderate-sized canyons (9,477 canyons in total), and significantly rectified the prior issue of grouping canyons together. Over 50% of the canyons identified in Harris et al. (2014) were not identified in Harris and Whiteway (2011), lending support to the use of this improved geomorphic data set. While this data set may still be missing some small-scale submarine canyons, it has sufficient resolution to capture the vast majority of submarine canyons existing in the ocean and makes a calculation of internal tide dissipation for all submarine canyons possible.

1.4. Physical Basis for Parameterization

Our goal in this study is to create an algorithm to determine the dissipation within each submarine canyon and to estimate the magnitude of the globally integrated canyon-driven dissipation, using a global internal tide model. While previous studies have sought to understand the mechanisms by which remotely-generated, M_2 -frequency, normally incident internal tides break and mix in canyons, this study focuses solely on the application of these results to the global inventory of canyons. To do so, we use the results from the idealized simulations of Nazarian and Legg (2017a, 2017b), which examined dissipation as a function of canyon geometric parameters. For a full description, we encourage the reader to refer to the papers which are available as open access; here we summarize and synthesize the pertinent results to create a parameterization for this present work.

In addition to diagnosing dissipative processes, Nazarian and Legg (2017a, 2017b) explored the relationship between the internal wave-driven dissipation and several geometric and wave parameters (canyon aspect ratio, ζ , canyon height, H , total ocean depth, D , canyon length, L , and the wavelength of the incident internal tide, λ_H). We express the canyon aspect ratio as

$$\zeta = \tan^{-1}(2L/W) \quad (2)$$

where W is the canyon width. Small values of ζ denote wide canyons while large values of ζ denote narrow canyons (see Figure 1 for a schematic of all geometric variables and Figure 5 for the range of ζ that occurs in nature). Two classes of idealized, V-shaped canyons were considered, differing only in sidewall steepness: near-critical slope canyons (with near-critical thalweg and supercritical sidewalls) and flat bottom canyons (with vertical sidewalls), both of which are illustrated in Figure 1.

Nazarian and Legg (2017a, 2017b) first conducted a parameter sweep over a range of aspect ratios (ζ). Both the turbulent dissipation and the divergence of the energy flux were calculated to determine the fraction (between 0 and 1) of the incoming internal tide's energy that was lost to mixing (see figure 6 of Nazarian & Legg, 2017b). In other words, they took the ratio of the energy lost (calculated from both the flux divergence and the explicitly diagnosed dissipation) in the simulation with canyon

topography to the incident energy flux in the simulation without topography. For the purposes of the current study, we average the energy loss diagnostics (turbulent dissipation and divergence of the energy flux) for each class of canyon (near-critical slope canyon or flat bottom canyon) at every aspect ratio and fit the averages with a cubic spline so that we can calculate the relative energy loss as a function of aspect ratio, $f(\zeta)$, for any value of aspect ratio, ζ . For clarity, we recreate Figure 6 from Nazarian and Legg (2017b) with the cubic spline of relative energy loss fit, $f(\zeta)$, superimposed in Figure 2. In the idealized simulations of Nazarian and Legg (2017b), there was strong nonlinear refraction (see their Figure 15) of the incoming

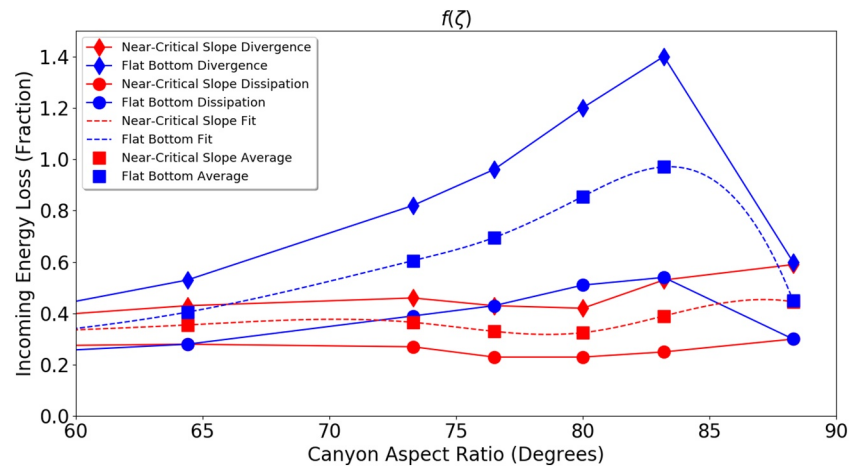


Figure 2. Fraction of the incident internal tide energy loss in two classes of idealized canyons: near-critical slope canyons (red) and flat bottom canyons (blue) as a function of the aspect ratio, ζ , from Nazarian and Legg (2017a, 2017b). The divergence of the energy flux (diamonds) and turbulent dissipation (circles) are averaged at each value of ζ (squares) and fit with a cubic spline to calculate $f(\zeta)$ for the global distribution of canyons (dashed line). We average the divergence and dissipation values here since there was a negligible conversion in prior idealized simulations (see Figure 4 of Nazarian & Legg, 2017b).

internal tide at high values of ζ , resulting in additional incoming internal tide energy flux entering the canyon mouth at the expense of adjacent regions. This mechanism led to a value of the divergence of the energy flux scaled by the incoming energy flux in the absence of topography that exceeded unity; the dissipation, however, was always less than or equal to the incoming flux. We only consider the cubic spline fit for the purposes of this study, and refer the reader to Nazarian and Legg (2017b) for a full discussion of the energetics.

In addition to considering the canyon aspect ratio (ζ) and sidewall steepness (near-critical slope canyon and flat bottom canyon), Nazarian and Legg (2017a) further considered the effects of canyon height, depth, length, and wavelength of the incident internal tide. Note that while these parameters influenced the total turbulent dissipation occurring within/around the canyon, the physical processes by which this dissipation occurred did not change. The first set of sensitivity studies in Nazarian and Legg (2017a) showed that the spatial extent of instability, and therefore mixing, within canyons scales approximately linearly with the relative canyon height (see Figure 13 of Nazarian & Legg, 2017a). This increase is bounded, however, since (a) the canyon height can never extend the overall depth of the water column, at which point none of the internal tides is able to propagate over the canyon onto the continental shelf and (b) for small canyon heights, little to no topographic reflection, and therefore dissipation occurs. The physical processes that lead to this scaling are elucidated using ray tracing; the wave rays are more likely to encounter the canyon walls for large canyons (large H/D) and ultimately dissipate, while wave rays are more likely to propagate onto the shelf without entering the canyon for small canyons (small values of H/D).

Similarly, the final sensitivity study of Nazarian and Legg (2017a) shows that the spatial extent of instability, and therefore mixing, within canyons scales approximately linearly with length (see Figure 14 of Nazarian & Legg, 2017a). Again, this increase is bounded, as the wavelength of the incoming internal wave also modulates the spatial extent of dissipation (Figure 14c of Nazarian & Legg, 2017a). Therefore, the spatial extent of instability, and thus total energy loss, also scales approximately like the ratio of the canyon length to the wavelength of the incident internal wave. Again, the ray tracing argument from that paper can be used to understand the physics; long canyons are more likely to have numerous reflections (large L/λ_H), whereas in small canyons the internal tide is likely to propagate out of the canyon after one reflection (small L/λ_H). This length dependence was corroborated by Hamann et al. (2021), Petrucio et al. (1998), and Waterhouse et al. (2017) who observed enhanced dissipation within canyons due to standing waves/seiches. In summary, Nazarian and Legg (2017a, 2017b) provide the following information for a parameterization: the fraction of energy dissipated in a canyon depends on aspect ratio ζ (from Figure 2) and scales linearly with H/D and L/λ_H .

1.5. Goals and Organization

The goal of this paper is to provide a global estimate of internal tide dissipation in canyons, using a parameterization based on the Nazarian and Legg (2017a, 2017b) results and incorporating canyon geometry data and internal tide model data. In Section 2, we use the previously summarized results from Nazarian and Legg (2017a, 2017b) to construct the parameterization used in this study. Furthermore, we provide a description of the various data used in the parameterization. We then discuss the results of this study in Section 3 and place them in the context of existing observations and our understanding of global ocean mixing in Section 4.

2. Methods and Data

2.1. Parameterization

To construct a parameterization of internal wave-driven dissipation in canyons, we utilize the aforementioned results from Nazarian and Legg (2017a, 2017b). This parameterization only includes the effects of reflection processes, namely scattering to higher wavenumbers and focusing, which are found to be the primary mechanisms for canyon-driven mixing in a number of observations and modeling studies. We propose that the total canyon-induced dissipation can be cast as

$$E \propto \left(\frac{H}{D}\right) \left(\frac{L}{\lambda_H}\right) f(\zeta) \mathcal{F}_{zi} W \quad (3)$$

where $f(\zeta)$ is the cubic spline of relative energy loss fit and \mathcal{F}_{zi} is the depth-integrated, normally-incident internal tide energy flux (all geometric parameters, H , D , L , W , and ζ , are illustrated in Figure 1 for clarity). In other words, the first three terms of Equation 3 determine the fraction of the incident internal tide energy that is dissipated in the canyon. When these terms are multiplied by the final two terms, which provide the rate of incident internal tide energy, we get the energy dissipated within the canyon. Specific values of $H/D = 0.50$ and $L/\lambda_H = 0.26$ were used in the simulations of Nazarian and Legg (2017b) from which we obtained $f(\zeta)$, so we normalize (3) by these values to derive a parameterization in terms of variables H , D , L , and λ_H :

$$E = \frac{1}{0.50 \times 0.26} \left(\frac{H}{D}\right) \left(\frac{L}{\lambda_H}\right) f(\zeta) \mathcal{F}_{zi} W \quad (4)$$

The total calculated energy dissipated in the canyon should never exceed the rate at which energy enters the canyon, so if the product of the first four terms in Equation 4 exceeds one, we set the product equal to unity (the condition is met for approximately 25% of the canyons included in this analysis). With this framework, we use existing data to determine the canyon geometric properties (H , D , L , ζ , and W) and the incident internal tide properties (λ_H and \mathcal{F}_{zi}). Note that the fraction of the canyon-induced energy loss as a function of ζ , $f(\zeta)$, is different for near-critical slope and flat bottom canyons (as illustrated in Figure 2). The topographic variables that we utilize throughout this study, and described in the next section, are bulk quantities for entire canyons, so we are unable to calculate how the slope, and thus the criticality, vary throughout the canyon. We are therefore unable to quantify whether each canyon is a near-critical slope canyon or flat bottom canyon and instead complete our calculation of Equation 4 twice; once assuming that all canyons are near-critical slope canyons and once assuming that all canyons are flat bottom canyons.

2.2. Submarine Canyon Data

Our parameterization requires topographic parameters H , D , L , W , and ζ (as stated in 1.3). We use the Harris et al. (2014) global seafloor geomorphic features map, which is derived from SRTM 30-arc s database (Becker et al., 2009). Only canyon bathymetry is considered. The canyon aspect ratio is calculated using Equation 2, where both the width, W , and length, L , are directly calculated by Harris et al. (2014). The canyon height, H , is similarly calculated by Harris et al. (2014), but the depth, D , is not directly calculated in the seafloor geomorphic features map. To calculate D , we take the sum of one half of the canyon height, H , and the mean depth of the entire canyon, D_{mean} (i.e., $D = \frac{1}{2}H + D_{\text{mean}}$). This provides the mean depth of the water column at the canyon which is consistent with the definition of D for this parameterization.

2.3. Internal Tide Fields

In addition to the topographic data, internal tide fields are necessary to calculate the internal tide-driven energy loss in each canyon, as estimated in Equation 4. Internal tide fields are calculated from a $1/25^\circ$ global HYCOM simulation with realistic tidal, buoyancy, and wind forcing (Buijsman et al., 2020). HYCOM is chosen for this study because the HYCOM fields and diagnosed internal tide energy fluxes have been robustly validated against observations over a range of frequency bands (Arbic et al., 2010, 2018; Ansong et al., 2015, 2017; Buijsman et al., 2020; Luecke et al., 2020). To conduct our analysis, we take the stratification and the M_2 harmonically-fitted sea surface height amplitude for the first mode from the HYCOM simulations. All data is taken from 2 weeks in September 2016 (once the model has been spun up and in a quasi-steady state, a period of a few years). We do not consider a longer time period due to data storage limitations (see Section 2.1 of Buijsman et al., 2020). Buijsman et al. (2020) show that, even for two weeks, there is good agreement between the HYCOM simulation and satellite altimetry. The effect of seasonal variability is not very large. Kaur and Buijsman are currently analyzing a time series with a duration of 6 years from an older $1/12^\circ$ global HYCOM simulation (Shriver et al., 2012). They find that the seasonal variance in the stationary M_2 internal tide sea surface height is on average 4.3% of the total variance for seafloor depths less than 2,000 m and 6.3% for seafloor depths greater than 2,000 m. These numbers are in agreement with Zaron and Egbert (2014), who found that about 10% of the variance in the mode-1 phase speed of internal tides around the Hawaiian Ridge can be attributed to seasonal variability.

While net fluxes from HYCOM could be taken from Buijsman et al. (2020), we calculate the incident flux using the plane wave fit methodology of Chiswell (2006) and Zhao et al. (2011) since our parameterization (4) defines F_{zi} as the normally-incident flux and not the net flux (we refer the reader to Figure 10 of Buijsman et al., 2020 for a diagram of the mode-1 net flux). The calculation of the depth-integrated energy flux involves three principle steps. First, we use real and imaginary components of the HYCOM steric sea surface height to find the amplitude (η) and direction of the three largest amplitude M_2 -frequency internal tides at the location of each canyon mouth during the 2-week period of the HYCOM simulation. This is an application of the plane wave fit that has been developed by Chiswell (2006), Zhao et al. (2011, 2016) rather than a novel advancement of the methodology, so we refer the interested reader to these papers for full details regarding this step (a good illustration of the extraction process for the three largest amplitude M_2 -frequency internal tides is provided in Figure 2 of Zhao et al., 2016). Second, we use the stratification at the canyon mouth to solve the Sturm-Liouville equation (equation below) to solve for the mode-1 eigenvalues and eigenfunctions. Third, we combine the eigenfunction with the wave amplitude to calculate the depth-integrated flux for each of the three most energetic waves. Based on these steps, this analysis only considers the mode-1, M_2 -frequency internal tides, consistent with the setup of Nazarian and Legg (2017a, 2017b) used to construct this parameterization.

Mathematically, steps two and three of the process to estimate the depth-integrated energy flux are conducted as follows. We solve the Sturm-Liouville equation, which can be cast as

$$\frac{\partial^2 \Phi_n(z)}{\partial z^2} + \frac{N^2(z)}{c_n^2} \Phi_n(z) = 0 \quad (5)$$

where z is the vertical coordinate, $\Phi_n(z)$ is the mode- n eigenfunction that describes both the vertical structure of displacement and vertical velocity, N^2 is the density stratification, and c_n is the mode- n eigenvalue (in this context, it is the mode- n eigenspeed). Boundary conditions of $\Phi_n(0) = \Phi_n(-H) = 0$, where H is the ocean depth, are used. The eigenspeed is related to the horizontal wavenumber by

$$c_n = \frac{\sqrt{\omega^2 - f^2}}{k_n} \quad (6)$$

where ω is the internal tide frequency, f is the Coriolis frequency, and k_n is the mode- n horizontal wavenumber. Solving (6) for k_n , the wavelength is calculated as $\lambda_H = 2\pi/k_n$. Note that we are neglecting the influence of internal tide refraction due to ambient currents and their shear (Duda et al., 2018); an estimate of the effects of refraction due to currents in HYCOM can be found in Buijsman et al. (2017).

To prevent aliasing, we conduct the plane wave fit using a window of one wavelength in both longitude and latitude. If any of the gridboxes contain land, the algorithm shifts toward the open ocean until all grid boxes in the window contain ocean tiles, before conducting the plane wave fit. At each canyon, we input model stratification from the center of the window into (5) to solve for the mode-1 eigenfunction $\Phi_1(z)$. The vertical structure of displacement and vertical velocity, $\Phi_n(z)$, can be related to the vertical structure of baroclinic pressure and horizontal velocity, $\Pi_n(z)$, by

$$\Pi_n(z) = \rho_0 c_n^2 \frac{d\Phi_n(z)}{dz} \quad (7)$$

where ρ_0 is the reference density. The corresponding sea surface displacement, a_n , is calculated as

$$a_n = \frac{\eta \rho_0 g}{\Pi_n(0)} \quad (8)$$

with η the amplitude of the mode- n internal tide calculated from the plane wave fit and g the acceleration due to gravity. Following the convention of LeBlond and Mysak (1978), the tidally averaged potential and kinetic energies can be written as

$$\langle \text{PE} \rangle = \frac{a_n^2 k_n^2}{4 (\omega^2 - f^2)} \int_{-H}^0 \frac{\Pi_n^2(z)}{\rho_0} dz \quad (9)$$

$$\langle \text{KE} \rangle = \frac{a_n^2 k_n^2 (\omega^2 + f^2)}{4 (\omega^2 - f^2)^2} \int_{-H}^0 \frac{\Pi_n^2(z)}{\rho_0} dz \quad (10)$$

Finally, the depth-integrated flux (in W/m) can be solved as $F_z = c_g \langle \text{PE} + \text{KE} \rangle$, which yields

$$F_z = \frac{a_n^2 \omega k_n}{2 (\omega^2 - f^2)} \int_{-H}^0 \frac{\Pi_n^2(z)}{\rho_0} dz \quad (11)$$

This process is conducted for each of the three most energetic waves, resulting in three fluxes and three propagation angles at each canyon location.

Since the depth-integrated flux calculated in Equation 11 is not necessarily oriented along the canyon axis, we take the projection of each of the three energy fluxes (the direction of each wave is calculated in the plane wave fit) in the direction of the canyon axis to determine the incident depth-integrated energy flux (i.e., entering the canyon through the mouth), F_{zi} . This projection is required because Equation 4 was created assuming the internal tides are normally incident. We then add the projected energy fluxes together from the three individual waves to get the total incident flux at the canyon mouth. Finally, this incident flux is multiplied by the canyon width, W , in Equation 4 to calculate the total power available within each canyon for mixing (in units of W). We neglect 372 of the 9,477 canyons from our analysis because these canyons are in shallow regions (defined by a depth less than 250 m) where the plane wave fit methodology is not particularly reliable (Zhao et al., 2011, 2016).

3. Results

Given the canyon geometric parameters and incident internal tide fluxes, we are able to calculate the total energy loss for each canyon. In order to understand how the individual terms of Equation 4 impact the overall energy loss, we consider each of the terms in isolation before evaluating the product. While some of these variables are directly calculated by Harris et al. (2014), they are presented there as averaged quantities, and this analysis illustrates the range of each geometric parameter throughout the ocean.

We begin by presenting PDFs of the submarine canyon height (Figure 3a) and canyon mouth depth (Figure 3b). Most canyons span a large vertical distance (many canyons have a vertical expanse greater than 1 km; see Figure 3a) and reside in relatively deep water (a majority of the canyons have a depth greater than 2 km; see Figure 3b). Therefore, while many of these submarine canyons are incised in the continental slope, they are open to the ocean interior at depth.

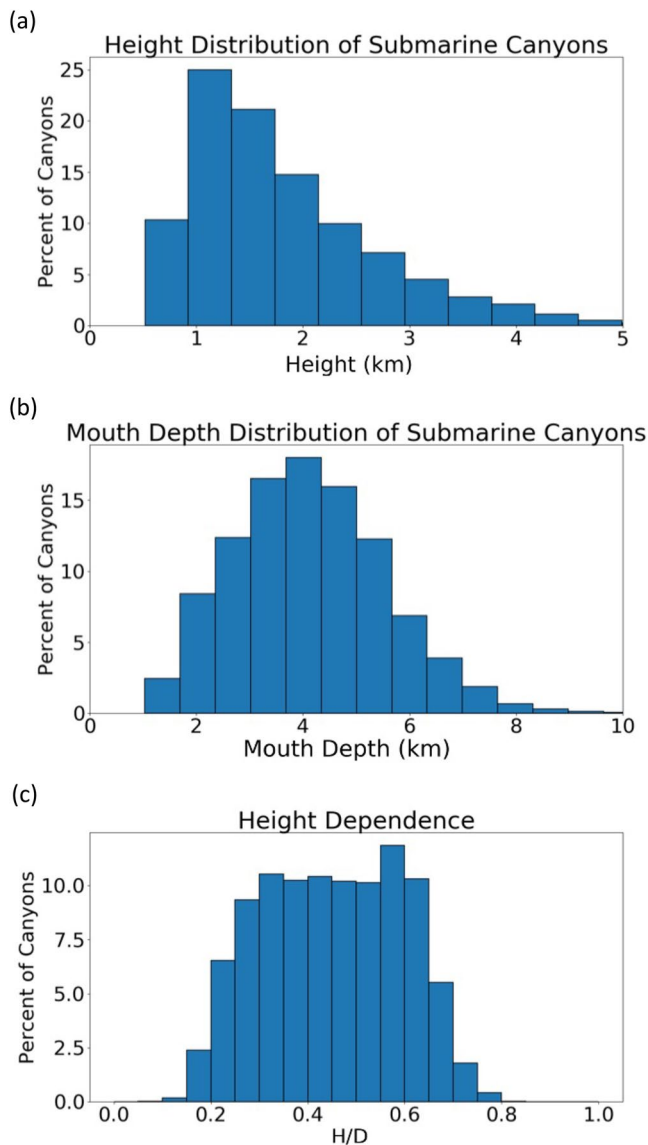


Figure 3. Distribution of submarine canyons based on (a) their height (H) as well as (b) the depth of the canyon mouth (D), and (c) their relative height (H/D). The majority of canyons span at least a kilometer in the vertical and reside in deeper waters. On average, canyons comprise one-half of the water column.

We now consider the first term of Equation 4: the ratio of the canyon height, H (Figure 3a), to the water column depth at the canyon, D (Figure 3b). Figure 3c illustrates that most canyons have a vertical extent that is approximately one-half of the total water column height, which is consistent with the idealized canyons constructed in Nazarian and Legg (2017a, 2017b). Canyons with a ratio of H/D greater than one-half dissipate the same fraction or a larger fraction of the incoming internal tide energy flux than those of Nazarian and Legg (2017a, 2017b), and are generally more favorable for dissipation, as dissipation scales like H/D .

The second term of Equation 4 compares the length of the canyon, L , to the horizontal wavelength of the incoming internal tide taken at each canyon, λ_H . The average value of the horizontal wavelength at submarine canyons in the high-resolution HYCOM simulations is 118 km, which is comparable with previous observations of internal tides in the deep ocean having wavelengths at the M_2 frequency of approximately 160 km (Rainville et al., 2010; Ray & Zaron, 2016; Zhao et al., 2011). The agreement between the wavelength at the canyons in this study and the observations of Rainville et al. (2010), Ray and Zaron (2016), and Zhao et al. (2011) is unsurprising since Figure 3b illustrates that canyons reside in relatively deep water. Figure 4 illustrates the PDF of values for L/λ_H for the distribution of global canyons. Note that the average value of L/λ_H for the global distribution of canyons is comparable with that of Nazarian and Legg (2017a, 2017b), and the distribution of L/λ_H is narrower than the distribution of H/D .

In addition to the contribution of the canyon height and length to the fraction of internal tide energy dissipated, the canyon aspect ratio, ζ , contributes to the dissipation of incoming tides. In Figure 5, we present the occurrences of values of ζ for the global distribution of canyons. All canyons in the Harris et al. (2014) data set have an aspect ratio greater than 60° , indicating that canyons are relatively narrow. Based on the parameterization presented in Figure 2, this would indicate that a significant fraction of the incoming internal tide's energy is dissipated in the canyon because $f(\zeta)$ is at a maximum when ζ is large (i.e., narrow canyons) for both near-critical and flat bottom canyons.

Now that we have considered all of the parameters that modulate the fraction of incoming energy lost in these canyons (the first three terms of Equation 4), we present global plots of the fractional energy loss for the flat bottom and near-critical slope canyons in Figures 6a and 6b, respectively. For the case of near-critical slope canyons (Figure 6b), there is a wide range of fractional energy loss that occurs; some canyons, such as those incising the Hawaiian Ridge, dissipate approximately 30% of the incident internal wave, whereas other canyons, such as those along the East

Coast of the United States, dissipate most (70%–100%) of the incident internal wave. The assumption that all global submarine canyons are flat bottom canyons leads to a higher fractional energy loss throughout the ocean (Figure 6a). The only difference in the two calculations presented in these plots is $f(\zeta)$, which is the energy loss function for near-critical slope and flat bottom canyons. The difference between the fractional energy loss assuming all canyons are flat bottom canyons and assuming all canyons are near-critical slope canyons is presented in Figure 6c. On average, the energy loss computed for a canyon under the assumption of flat bottom topography is 10%–40% larger than the energy loss computed for a canyon under the assumption of near-critical slope topography. As previously stated, submarine canyons are neither perfectly flat bottom nor near-critical slope, but conducting this analysis twice allows us to formulate a realistic range of internal tide energy dissipated in submarine canyons.

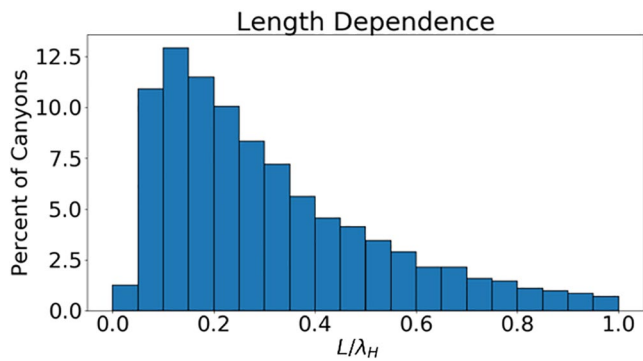


Figure 4. Distribution of submarine canyons based on their relative length (L/λ_H). λ_H is the incident internal wavelength at each canyon mouth. For the majority of canyons, the canyon length is one order of magnitude smaller than the wavelength of the impinging internal tide.

Before calculating the canyon-induced energy loss, we additionally consider the incoming, depth-integrated internal tide flux at each canyon mouth, \mathcal{F}_{zi} , as diagnosed from the plane wave fit of the $1/25^\circ$ HYCOM simulation. The global map of incident, mode-1, M_2 -frequency, depth-integrated flux is presented in Figure 7. We expect that regions of low flux will also be regions of low energy loss. We consider the internal tide flux and the total energy loss at each canyon together in the analysis that follows.

Based on the presented geometric variables and internal tide energy fluxes from HYCOM, we calculate the energy loss in individual canyons. Results are presented in Figures 8a and 8b under the assumption that all canyons are either flat bottom or near-critical slope, respectively, and are plotted spatially to provide insight into the distribution of canyon-driven mixing. Note that the spatial pattern of dissipation is comparable between Figures 8a and 8b, but, on average, more energy loss is experienced when we assume all submarine canyons to be flat bottom canyons (Figure 8a) than when we assume all submarine canyons to be near-critical slope canyons

(Figure 8b). Globally, if we assume all canyons have near-critical slope, we calculate approximately 43.8 GW of internal tide energy loss, while if we assume all canyons are flat-bottomed, we calculate approximately 58.1 GW of internal tide energy loss. Considering the seasonal variability reported in Section 2.3, the range of parameterized energy loss expands to 30.8–75.3 GW.

Figure 8 illustrates that the magnitude of canyon-driven dissipation has a significant spatial dependence. Canyons in low and mid-latitudes dissipate, on average, 10^7 W, while canyons at high latitudes dissipate significantly less; approximately 10^4 W. These high latitudes are beyond the critical latitude (74.5°) for mode-1, M_2 -frequency internal tides and have a low incident flux as seen in Figure 7. Instead, these regions primarily have lower energy, high-frequency internal tides. Additionally, submarine canyons in the Mediterranean Ocean experience less dissipation than the global average due to the small local internal tide flux, which can likewise be seen in Figure 7.

The parameterized canyon-driven dissipation rates are summarized by region in Table 1. The percent of the incident internal tide energy dissipated, the dissipation in GW, and the percent of dissipation relative to the global canyon dissipation are presented for each region. Values are presented as the average of the near-critical slope and flat bottom canyon calculations. Regions with a high percentage of the incident internal tide dissipated, such as the South or North Atlantic, do not necessarily have the largest percent of canyon-induced dissipation globally since (a) there are relatively few canyons in these regions and (b) the depth-integrated incident flux is relatively small in these regions (see Figure 7). Rather, regions with canyons that dissipate a smaller fraction of the incident internal tide but are more abundant and/or experience higher internal tide flux, are the primary contributor to internal tide dissipation.

4. Discussion and Conclusions

In order to test the robustness of our results, we compare energy loss calculated from five sets of observations with our parameterized energy loss following the framework of Hamann et al. (2021). Specifically, Hamann et al. (2021) used published observations of the La Jolla Canyon System [117.3 W, 32.9 N] (Alberty et al., 2017; Hamann et al., 2021), Monterey Canyon [121.9 W, 36.8 N] (Wain et al., 2013), Ascension Canyon [122.5 W, 36.9 N] (Gregg et al., 2011), Eel Canyon [124.7 W, 40.6 N] (Waterhouse et al., 2017), Gaoping Canyon [120.2 E, 22.3 N] (Lee et al., 2009), and Juan de Fuca Canyon [125.5 W, 48.0 N] (Alford et al., 2014) to compare the incoming internal tide flux and the canyon-integrated energy loss. We have replicated this observation-based estimate and superimposed the flux derived from our plane wave fit and the corresponding energy loss diagnosed from our parameterization for the La Jolla Canyon System, as well as Monterey, Ascension, Eel, and Gaoping Canyons and present the results in Figure 9. We do not consider Juan de Fuca Canyon in our comparison since the observed energy loss in the canyon exceeds the incoming flux, which is not allowed in our parameterization. Error bounds for the parameterized energy loss are calculated as the

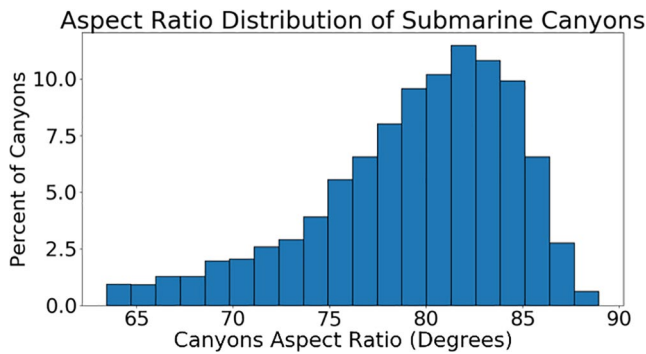


Figure 5. Distribution of submarine canyons based on their aspect ratio, ζ . The majority of canyons are narrow. Based on the fit presented in Figure 2, this narrowness suggests that these canyons may dissipate a significant amount of the incoming internal tide's energy.

sum of the seasonal variability, presented in Section 2.3, and the difference in energy loss calculated between the flat bottom and near-critical slope canyon by the parameterization in Equation 4.

For four of the five canyons that we consider, the plane-wave, incident flux and parameterized canyon-integrated energy loss are of the same order of magnitude as the corresponding fields calculated from observations (Monterey, Ascension, Eel, and Gaoping Canyons). The parameterized energy loss in Gaoping Canyon is consistent with observations, to within error bars, and the parameterized energy loss in Eel Canyon is nearly comparable with observations when including the error bars. For both Ascension and Monterey Canyons, the parameterized energy loss is within a factor of four of the observed energy loss without any consideration of the observational or model error. Additionally, both the parameterized and observed canyon-integrated energy loss for all canyons lie on or close to the one-to-one line, illustrating that almost all, if not all, of the incoming internal tide, is dissipated within the canyon. Based on the data presented in Table 1, most submarine canyons do not dissipate all of the

incident internal tide, making these canyons particularly efficient. The La Jolla Canyon System is an outlier, for which our parameterization diagnosed an incoming flux and canyon-integrated dissipation that is one order of magnitude smaller than that observed. We hypothesize that this order of magnitude difference for the La Jolla Canyon System is due to the plane wave fit; notably, the plane wave fit technique has less skill in shallow water (Zhao et al., 2011, 2016). The mouth of the La Jolla Canyon System has a depth of approximately 500–600 m, the threshold at which the plane wave fit starts to fail, whereas the other canyons considered here have depths approximately 1 km or larger. Additionally, unlike the observations showing nearly 100% of the incoming energy being dissipated, the parameterization prescribes only partial dissipation. This may be attributed to the modal structure in La Jolla Canyon System. Observations show that the dominant modes are 2 and higher. If this were accounted for in the parameterization, the shorter horizontal wavelength would lead to a larger fraction of the incident energy being lost to local mixing. This failure of the plane wave fit at shallow canyons is not significant, however, since the vast majority of submarine canyons taken from the Harris et al. (2014) study have a canyon mouth depth exceeding 1 km (Figure 3b).

To put this estimate of submarine canyon-driven mixing into the context of the global energy budget, we consider the total power in the internal tide field. Based on the high-resolution HYCOM simulations of Buijsman et al. (2020), approximately 970 GW of power is available in the global M_2 -frequency internal tide field for mixing (both low and high modes). Summing the dissipation occurring in all canyons and accounting for seasonal variability, we estimate a power loss of 30.8–75.3 GW which suggests that 3.2%–7.8% of the M_2 -frequency internal tide field is dissipated within submarine canyons (all frequencies and all modes). Furthermore, we use the calculations of dissipation from the framework of de Lavergne et al. (2019) to consider the M_2 component of the internal tides. In their framework, de Lavergne et al. (2019) calculate that 5% of the M_2 -frequency internal tide field (modes 1–5) dissipates over shelves and 15% of the M_2 -frequency internal tide field (modes 1–5) dissipates over critical slopes. Comparing these values to the estimate of 3.2%–7.8% of the M_2 -frequency internal tide field dissipated in canyons suggests that canyons are just as important as shelves in dissipating the M_2 internal tides and may account for a significant fraction of the dissipation due to critical slopes.

The range of internal tide power dissipation in canyons presented here is higher than that extrapolated from single observations of canyons. While canyons on both coasts of the United States have a non-negligible energy loss, Figure 8 and Table 1 show that canyons in the Oceania region/Asian Seas and the Indian Ocean are responsible for dissipating the most energy and canyons off both coasts of the United States dissipate, on average, less energy than the average dissipation of all submarine canyons. This suggests that prior calculations of globally integrated, canyon-induced energy loss based on observations of Monterey Canyon (Carter & Gregg, 2002; Gregg et al., 2005) may be underestimates of the total canyon-induced energy loss (they approximated 15 GW of energy input into the global internal tide field is dissipated in canyons, whereas our parameterization suggests that this value is close to 30.8–75.3 GW, which is two to five times

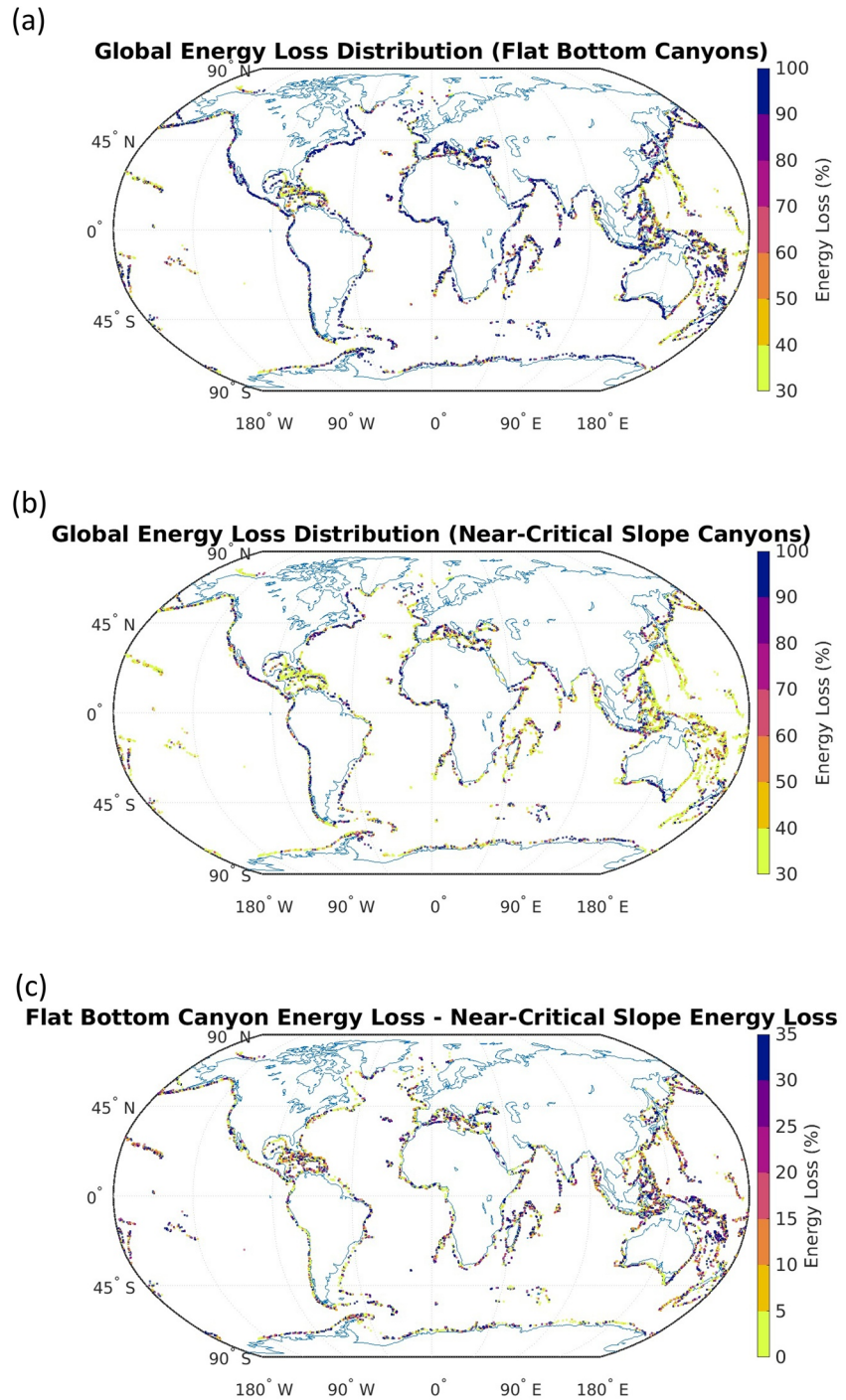


Figure 6. Percent of the incoming internal wave energy dissipated in submarine canyons, as calculated by the first three terms of Equation 4 assuming that all canyons are (a) flat bottom canyons or (b) near-critical slope canyons. (c) The difference in the percent of incident energy loss between the flat bottom and near-critical slope canyons.

larger than their estimate). While Monterey Canyon is more efficient at dissipating the incident internal tide (almost all of the incident energy is deposited to mixing), the depth-integrated flux is relatively small compared to other regions of the ocean, which renders the dissipation in Monterey Canyon unrepresentative of the global mean. Therefore, while we expect the processes by which internal tides reflect off and mix in canyons from existing observations to be generalizable to the global distribution of canyons, our results

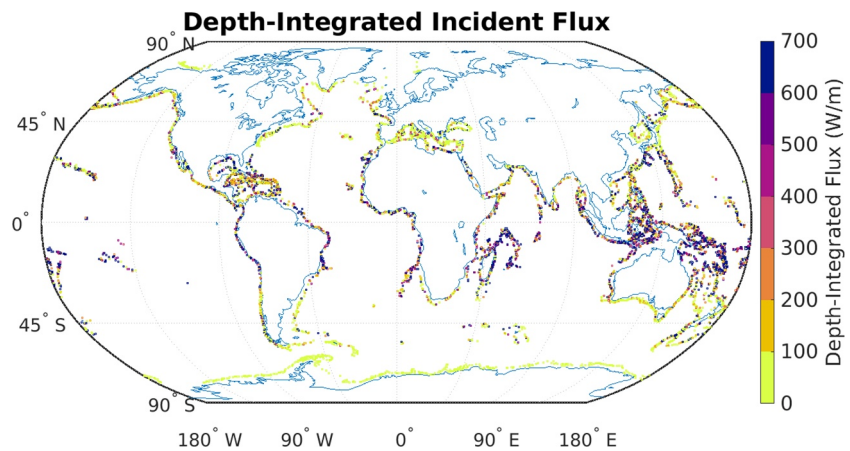


Figure 7. Incoming, mode-1, M_2 -frequency, depth-integrated internal tide flux at each canyon mouth taken from high-resolution HYCOM simulation.

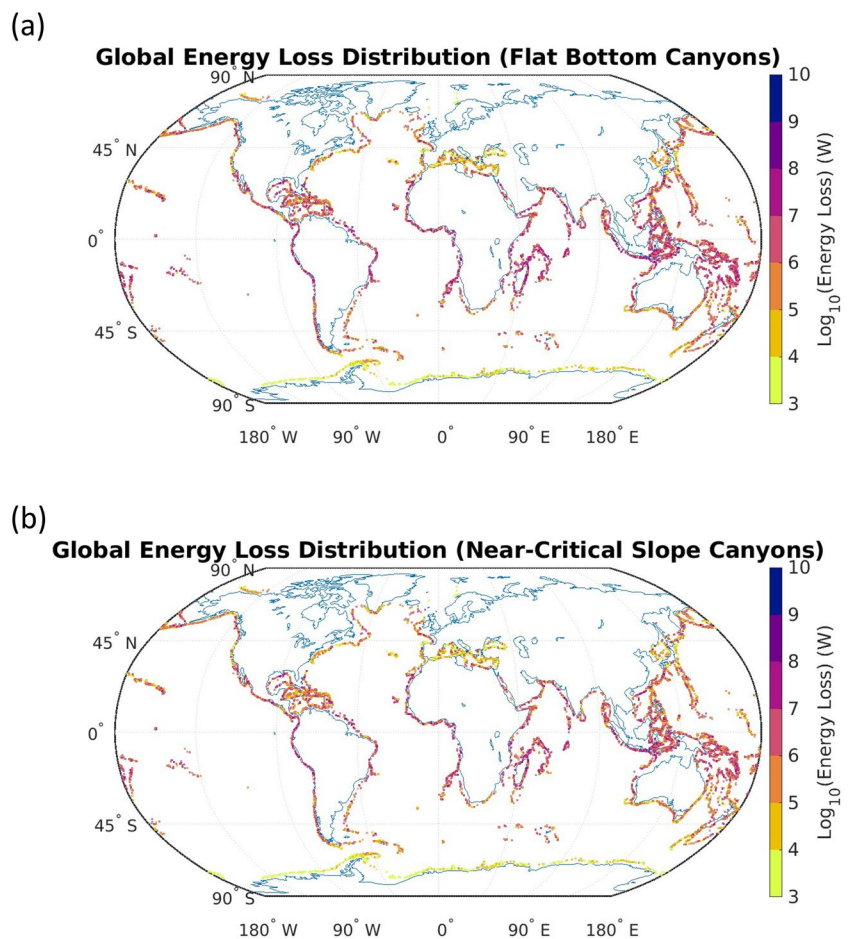


Figure 8. (a) Global distribution of canyon-induced energy loss under the assumption that all submarine canyons are flat bottom canyons. When summed over the global ocean, these canyons are responsible for dissipating 58.1 GW of energy from the internal tides. (b) Global distribution of canyon-induced energy loss under the assumption that all submarine canyons are near-critical slope canyons. When summed over the global ocean, these canyons are responsible for dissipating 43.8 GW of energy from the internal tides.

Table 1
Region-Averaged Percent of Incident Energy Loss, Absolute Energy Loss in GW, and Fraction of Global Energy Loss in Canyons

	% Incident Loss	Absolute loss (GW)	% Global Canyon Loss
Arabian Sea	64	0.62	1.2
Arctic Ocean	38	0.02	0.04
Caribbean Sea	44	5.6	11
Indian Ocean	56	8.9	17
Mediterranean Sea	57	1.4	2.7
North Atlantic Ocean	63	3.5	6.8
North Pacific Ocean	59	6.7	13
Oceania and Asian Seas	49	17	33
South Atlantic Ocean	67	2.2	4.3
South Pacific Ocean	62	3.6	7.0
Southern Ocean	58	1.6	3.1

Note. Results are calculated by taking the average of the energy loss diagnosed assuming all submarine canyons are near-critical slope canyons or all are flat bottom canyons.

suggest that canyon-integrated dissipation for observed canyons is lower than the global average.

Our goal in this work has been to estimate the globally-integrated turbulent dissipation in canyons due to remotely generated internal tides. While important, this is not the only dissipative mechanism in canyons, nor at the continental slope. Chief among the dissipative physical processes occurring in canyons that are missing from our parameterization are locally generated internal tides, supercritical bumps, flow separation, wind-driven upwelling, wave-wave interactions, nonlinear bores and fronts, warm-core rings, among many others. While each of these processes may contribute to the total dissipation occurring at each canyon, our goal here is to perform the first parameterization of canyon-induced mixing for all submarine canyons driven by the breaking of incoming internal tides, rather than accounting for every possible mechanism by which canyon-driven dissipation occurs. Additionally, while the canyon-driven dissipation we have diagnosed here is a significant process through which dissipation of internal tides occurs at the continental slope, it is not the only dissipative process. As diagnosed by Kelly et al. (2013) and de Lavergne et al. (2019), scattering off the continental slope, shoaling, and wave-wave interactions are additional significant contributors to dissipation at/on the continental slope/shelf. Nevertheless, the dissipation due to remotely generated internal tide reflection processes in canyons is non-negligible and serves as one of many processes by which mixing occurs at the ocean margins.

Although the range of global canyon-driven dissipation computed here is comparable to or larger than previous estimates, we anticipate that this range is an underestimate. While the 30-arc s database used to identify canyons by Harris et al. (2014) is high resolution, it is insufficiently high to capture all open ocean canyons. Furthermore, the idealized simulations of Nazarian and Legg (2017a, 2017b) show that, for canyons with a large aspect ratio ($\zeta \gtrsim 80^\circ$), there is nonlinear refraction of the incoming internal tide, such that there is an increased flux that enters the canyon mouth rather than reflecting off the abutting continental slope. For our narrowest canyons, this would increase the energy loss diagnosed from Equation 4 because the product of depth-integrated flux and width, $F_{zi}W$, does not take into account the additional flux into the canyon mouth due to this refraction. Taken together, these caveats indicate that we may be underestimating the canyon-induced dissipation, which is done purposefully to give a conservative estimate of canyon-induced dissipation.

In this study, we have considered the magnitude of energy loss in submarine canyons due to the reflection of internal tides. Using a high-resolution global canyon data set and a high-resolution tidal model, we have parameterized and calculated the energy dissipated in each submarine canyon due to the topographic scattering to higher modes and focusing on the impinging tides. By assuming that submarine canyons are either all near-critical slope canyons or all flat bottom canyons, we have estimated that submarine canyons are responsible for dissipating 30.8–75.3 GW of internal tide energy. Taken relative to the energy in the M_2 -frequency internal tide field, this is 3.2%–7.8%. This range of canyon-induced dissipation is greater than estimates of globally integrated dissipation from observations of individual canyons (Carter & Gregg, 2002; Gregg et al., 2005) and suggests that canyons may be more important sinks of internal tide energy than previously thought.

Figure 9. Canyon-integrated turbulent dissipation (kW) as a function of area-integrated incident flux (kW). The dashed line represents the condition when all of the incoming internal tide is dissipated in the canyon. Triangle markers represent plane wave flux calculation and corresponding parameterized (P) energy loss (with error bars representing the range of energy loss for near-critical slope and flat bottom canyons in addition to the seasonal variability) and diamond markers represent flux and dissipation data from observations (O).

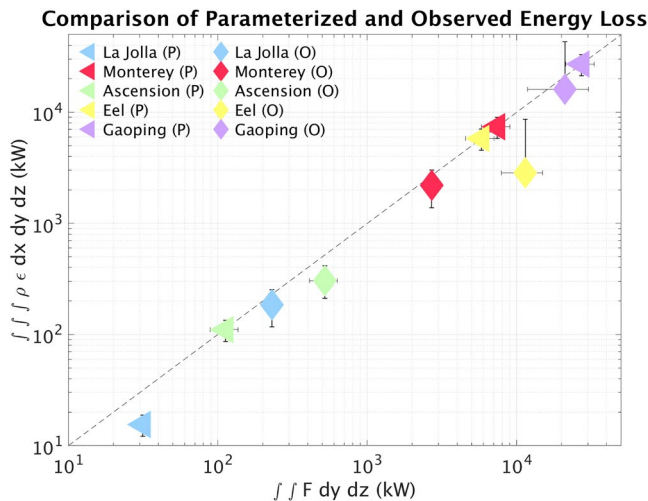


Figure 9. Canyon-integrated turbulent dissipation (kW) as a function of area-integrated incident flux (kW). The dashed line represents the condition when all of the incoming internal tide is dissipated in the canyon. Triangle markers represent plane wave flux calculation and corresponding parameterized (P) energy loss (with error bars representing the range of energy loss for near-critical slope and flat bottom canyons in addition to the seasonal variability) and diamond markers represent flux and dissipation data from observations (O).

Given that the magnitude of dissipation calculated in this work is of the same order of magnitude as the dissipation due to locally generated internal tides, which is already included in ocean models, we expect that there will be implications for the modeled ocean state and mean circulation (Melet et al., 2016). Additionally, this work only considers the horizontal distribution of canyons and dissipation and not the vertical distribution of dissipation within the canyon. Future studies examining the vertical distribution of dissipation within canyons will be essential, as the vertical distribution of dissipation is far more important for the large-scale ocean circulation and water mass transformation than the horizontal distribution of dissipation (Melet et al., 2016). Future work parameterizing the global dissipation due to all dissipative processes, including the canyon-induced component, is therefore paramount in the creation of more physical ocean models (Eden et al., 2014; de Lavergne et al., 2019; MacKinnon et al., 2017).

Data Availability Statement

The topographic data were obtained from Conservation International, GRID-Arendal, and Geoscience Australia (bluehabitats.org). The HYCOM fields used in this study were provided by M. Buijsman and are publicly-available at <https://doi.org/10.5281/zenodo.5514226>.

Acknowledgments

R. Nazarian and C. Burns gratefully acknowledge support from Fairfield University, including the College of Arts and Sciences and the Science Institute. R. Nazarian and C. Burns also gratefully acknowledge support from the NASA Connecticut Space Grant Consortium, award NNX15AI12H. Sonya Legg was supported under award NA18OAR4320123 from the National Oceanic and Atmospheric Administration, U.S. Department of Commerce. The statements, findings, conclusions, and recommendations are those of the author(s) and do not necessarily reflect the views of the National Oceanic and Atmospheric Administration, or the U.S. Department of Commerce. M. Buijsman acknowledges support from NASA Grant 80NSSC18K0771, US National Science Foundation (NSF) grant OCE-1537449, and Office of Naval Research (ONR) grant N00014-15-1-2288. B. Arbic acknowledges support from US National Science Foundation (NSF) grant OCE-1851164. The authors thank Zhongxiang Zhao for a useful discussion of the plane wave fit methodology. We are grateful for the comments of the associate editor and two anonymous reviewers, which greatly improved the manuscript.

References

- Alberty, M., Billheimer, S., Hamann, M., Ou, C., Tamsitt, V., Lucas, A., & Alford, M. (2017). A reflecting, steepening, and breaking internal tide in a submarine canyon. *Journal of Geophysical Research: Oceans*, *122*, 1882–1900. <https://doi.org/10.1002/2016jc012583>
- Alford, M., Klymak, J., & Carter, G. (2014). Breaking internal lee waves at kaena ridge, hawaii. *Geophysical Research Letters*, *41*, 906–912. <https://doi.org/10.1002/2013gl059070>
- Ansong, J., Arbic, B., Alford, M., Buijsman, M., Shriver, J., Zhao, Z., & Zamudio, L. (2017). Semidiurnal internal tide energy fluxes and their variability in a global ocean model and moored observations. *Journal of Geophysical Research: Oceans*, *122*, 1882–1900. <https://doi.org/10.1002/2016jc012184>
- Ansong, J., Arbic, B., Buijsman, M., Richman, J., Shriver, J., & Wallcraft, A. (2015). Indirect evidence for substantial damping of low-mode internal tides in the open ocean. *Journal of Geophysical Research: Oceans*, *120*, 6057–6071. <https://doi.org/10.1002/2015jc010998>
- Arbic, B., Alford, M., Ansong, J., Buijsman, M., Ciotti, C., Farrar, T., & Zhao, Z. (2018). A primer on global internal tide and internal gravity wave continuum modeling in hycom and mitgcm. *New Frontiers in Operational Oceanography*. <https://doi.org/10.17125/gov2018.ch13>
- Arbic, B., Wallcraft, A., & Metzger, E. (2010). Concurrent simulation of the eddy general circulation and tides in a global climate model. *Ocean Modelling*, *32*, 175–187. <https://doi.org/10.1016/j.ocemod.2010.01.007>
- Aslam, T., Hall, R., & Dye, S. (2018). Internal tides in a dendritic submarine canyon. *Progress in Oceanography*, *169*, 20–32. <https://doi.org/10.1016/j.pocean.2017.10.005>
- Becker, J., Sandwell, D., Smith, W., Braud, J., Binder, B., Depner, J., & Weatherall, P. (2009). Global bathymetry and elevation data at 30 arc seconds resolution: SRTM30_plus. *Marine Geodesy*, *32*, 355–371. <https://doi.org/10.1080/01490410903297766>
- Bosley, K., Lavelle, J., Brodeur, R., Wakefield, W., Emmett, R., Baker, E., & Rehmke, K. (2004). Biological and physical processes in and around astoria submarine canyon, Oregon, USA. *Journal of Marine Systems*, *50*, 21–37. <https://doi.org/10.1016/j.jmarsys.2003.06.006>
- Bruno, M., Vazquez, A., Gomez-Enri, J., Vargas, J., Lafuente, J., Ruiz-Canavante, A., & Vidal, J. (2006). Observations of internal waves and associated mixing phenomena in the portimao canyon area. *Deep-Sea Research*, *53*, 1219–1240. <https://doi.org/10.1016/j.dsr.2006.04.015>
- Bryan, F. (1987). Parameter sensitivity of primitive equation ocean general circulation models. *Journal of Physical Oceanography*, *17*, 970–985. [https://doi.org/10.1175/1520-0485\(1987\)017<0970:psopeo>2.0.co;2](https://doi.org/10.1175/1520-0485(1987)017<0970:psopeo>2.0.co;2)
- Buijsman, M., Arbic, B., Richman, J., Shriver, J., Wallcraft, A., & Zamudio, L. (2017). Semidiurnal internal tide incoherence in the equatorial pacific. *Journal of Geophysical Research: Oceans*, *122*, 5286–5305. <https://doi.org/10.1002/2016jc012590>
- Buijsman, M., Stephenson, G., Ansong, J., Arbic, B., Green, M., Richman, J., & Zhao, Z. (2020). On the interplay between horizontal resolution and wave drag and their effect on tidal baroclinic mode waves in realistic global ocean simulations. *Ocean Modelling*, *152*, 101656. <https://doi.org/10.1016/j.ocemod.2020.101656>
- Cacchione, D., Pratson, L., & Ogston, A. S. (2002). The shaping of continental slopes by internal tides. *Science*, *296*, 724–727. <https://doi.org/10.1126/science.1069803>
- Cacchione, D., & Wunsch, C. (1974). Experimental study of internal waves over a slope. *Journal of Fluid Mechanics*, *66*, 223–239. <https://doi.org/10.1017/s0022112074000164>
- Carter, G., & Gregg, M. (2002). Intense, variable mixing near the head of monterey submarine canyon. *Journal of Physical Oceanography*, *32*, 3145–3165. [https://doi.org/10.1175/1520-0485\(2002\)032<3145:ivmth>2.0.co;2](https://doi.org/10.1175/1520-0485(2002)032<3145:ivmth>2.0.co;2)
- Chiswell, S. (2006). Altimeter and current meter observations of internal tides: Do they agree? *Journal of Physical Oceanography*, *36*, 1860–1872. <https://doi.org/10.1175/jpo2944.1>
- Codiga, D., Renouard, D., & Fincham, A. (1999). Experiments on waves trapped over the continental slope and shelf in a continuously stratified rotating ocean. *Journal of Marine Research*, *57*, 585–612. <https://doi.org/10.1357/002224099321549602>
- de Lavergne, C., Falahat, S., Madec, G., Roquet, F., Nycander, J., & Vic, C. (2019). Toward global maps of internal tide energy sinks. *Ocean Modelling*, *137*, 52–75. <https://doi.org/10.1016/j.ocemod.2019.03.010>
- Duda, T., Lin, Y.-T., Buijsman, M., & Newhall, A. (2018). Internal tidal modal ray refraction and energy ducting in baroclinic Gulf Stream currents. *Journal of Physical Oceanography*, *48*, 1969–1993. <https://doi.org/10.1175/jpo-d-18-0031.1>
- Eden, C., Czeschel, L., & Olbers, D. (2014). Toward energetically consistent ocean models. *Journal of Physical Oceanography*, *44*, 3160–3184. <https://doi.org/10.1175/jpo-d-13-0260.1>
- Egbert, G., & Ray, R. (2000). Significant dissipation of tidal energy in the deep ocean inferred from satellite altimeter data. *Nature*, *405*, 775–778. <https://doi.org/10.1038/35015531>

- Eriksen, C. (1982). Observations of internal wave reflection off sloping bottoms. *Journal of Geophysical Research*, *87*, 525–538. <https://doi.org/10.1029/jc087ic01p00525>
- Gardner, W. (1989). Periodic resuspension in Baltimore canyon by focusing of internal waves. *Journal of Geophysical Research*, *94*, 18185–18194. <https://doi.org/10.1029/jc094ic12p18185>
- Gordon, R., & Marshall, N. (1976). Submarine canyons: Internal wave traps? *Geophysical Research Letters*, *3*, 622–624. <https://doi.org/10.1029/gl003i010p00622>
- Gregg, M., Carter, G., & Kunze, E. (2005). Corrigendum. *Journal of Physical Oceanography*, *35*, 1712–1715. <https://doi.org/10.1175/jpo2789.1>
- Gregg, M., Hall, R., Carter, G., Alford, M., Lien, R.-C., Winkel, D., & Wain, D. (2011). Flow and mixing in ascension, a steep, narrow canyon. *Journal of Geophysical Research*, *116*(C7). <https://doi.org/10.1029/2010jc006610>
- Hall, R., & Carter, G. (2011). Internal tides in Monterey submarine canyon. *Journal of Physical Oceanography*, *41*, 186–204. <https://doi.org/10.1175/2010jpo4471.1>
- Hamann, M., Alford, M., Lucas, A., Waterhouse, A., & Voet, G. (2021). Turbulence driven by reflected internal tides in a supercritical submarine canyon. *Journal of Physical Oceanography*, *51*, 591–609. <https://doi.org/10.1175/jpo-d-20-0123.1>
- Harris, P., Macmillan-Lawler, M., Rupp, J., & Baker, E. (2014). Geomorphology of the oceans. *Marine Geology*, *352*, 4–24. <https://doi.org/10.1016/j.margeo.2014.01.011>
- Harris, P., & Whiteway, R. (2011). Global distribution of large submarine canyons: Geomorphic differences between active and passive continental margins. *Marine Geology*, *285*, 69–86. <https://doi.org/10.1016/j.margeo.2011.05.008>
- Hotchkiss, F., & Wunsch, C. (1982). Internal waves in Hudson canyon with possible geological implications. *Deep-Sea Research*, *29*, 415–442. [https://doi.org/10.1016/0198-0149\(82\)90068-1](https://doi.org/10.1016/0198-0149(82)90068-1)
- Johnston, T., & Merrifield, M. (2003). Internal tide scattering at seamounts, ridges, and islands. *Journal of Geophysical Research*, *108*, 3180. <https://doi.org/10.1029/2002jc001528>
- Kelly, S., Jones, N., Nash, J., & Waterhouse, A. (2013). The geography of semidiurnal mode-1 internal-tide energy loss. *Geophysical Research Letters*, *40*, 4689–4693. <https://doi.org/10.1002/grl.50872>
- Klymak, J., Alford, M., Pinkel, R., Lien, R.-C., Yang, Y., & Tang, T.-Y. (2011). The breaking and scattering of the internal tide on a continental slope. *Journal of Physical Oceanography*, *41*, 926–945. <https://doi.org/10.1175/2010jpo4500.1>
- Kunze, E., MacKay, C., McPhee-Shaw, E., Morrice, K., Girton, J., & Terker, S. (2012). Turbulent mixing and exchange with interior waters on sloping boundaries. *Journal of Physical Oceanography*, *42*, 910–927. <https://doi.org/10.1175/jpo-d-11-075.1>
- LeBlond, P., & Mysak, L. (1978). *Waves in the ocean*. Elsevier Scientific Publishing.
- Lee, I.-H., Lien, R.-C., Liu, J., & Chuang, W.-S. (2009). Turbulent mixing and internal tides in Gaoping (Kaoping) submarine canyon, Taiwan. *Journal of Marine Systems*, *76*, 383–396. <https://doi.org/10.1016/j.jmarsys.2007.08.005>
- Legg, S. (2014). Scattering of low-mode internal waves at finite isolated topography. *Journal of Physical Oceanography*, *44*, 359–383. <https://doi.org/10.1175/jpo-d-12-0241.1>
- Leichter, J., Stewart, H., & Miller, S. (2003). Episodic nutrient transport to Florida coral reefs. *Limnology & Oceanography*, *48*, 1394–1407. <https://doi.org/10.4319/lo.2003.48.4.1394>
- Luecke, C., Arbic, B., Richman, J., Shriver, J., Alford, M., Ansong, J., & Zamudio, L. (2020). Statistical comparisons of temperature variance and kinetic energy in global ocean models and observations: Results from mesoscale to internal wave frequencies. *Journal of Geophysical Research: Oceans*, *125*, e2019JC015306. <https://doi.org/10.1029/2019jc015306>
- MacKinnon, J., Zhao, Z., Whalen, C., Waterhouse, A., Trossman, D., Sun, O., & Alford, M. (2017). Climate process team on internal wave-driven mixing. *Bulletin of the American Meteorological Society*, *2429*–2454. <https://doi.org/10.1175/bams-d-16-0030.1>
- McPhee-Shaw, E. (2006). Boundary interior exchange: Reviewing the idea that internal-wave mixing enhances lateral dispersal near continental margins. *Deep-Sea Research*, *53*, 42–59. <https://doi.org/10.1016/j.dsr2.2005.10.018>
- Melet, A., Legg, S., & Hallberg, R. (2016). Climatic impacts of parameterized local and remote tidal mixing. *Journal of Climate*, *29*, 3473–3500. <https://doi.org/10.1175/jcli-d-15-0153.1>
- Munk, W. (1966). Abyssal recipes. *Deep-Sea Research*, *13*, 207–230. [https://doi.org/10.1016/0011-7471\(66\)90602-4](https://doi.org/10.1016/0011-7471(66)90602-4)
- Munk, W., & Wunsch, C. (1998). Abyssal recipes ii: Energetics of tidal and wind mixing. *Deep-Sea Research*, *45*, 1977–2010. [https://doi.org/10.1016/s0967-0637\(98\)00070-3](https://doi.org/10.1016/s0967-0637(98)00070-3)
- Nazarian, R. (2018). *Internal wave scattering in continental slope canyons (Unpublished doctoral dissertation)*. Princeton University.
- Nazarian, R., & Legg, S. (2017a). Internal wave scattering in continental slope canyons, part 1: Theory and development of a ray tracing algorithm. *Ocean Modelling*, *118*, 1–15. <https://doi.org/10.1016/j.ocemod.2017.07.002>
- Nazarian, R., & Legg, S. (2017b). Internal wave scattering in continental slope canyons, part 2: A comparison of ray tracing and numerical simulations. *Ocean Modelling*, *118*, 16–30. <https://doi.org/10.1016/j.ocemod.2017.07.005>
- Petruncio, E., Rosenfeld, L., & Paduan, J. (1998). Observations of the internal tide in Monterey canyon. *Journal of Physical Oceanography*, *28*, 1873–1903. [https://doi.org/10.1175/1520-0485\(1998\)028<1873:ootiti>2.0.co;2](https://doi.org/10.1175/1520-0485(1998)028<1873:ootiti>2.0.co;2)
- Polzin, K., Toole, J., Ledwell, J., & Schmitt, R. (1997). Spatial variability of turbulent mixing in the Abyssal ocean. *Science*, *276*, 93–96. <https://doi.org/10.1126/science.276.5309.93>
- Rainville, L., Johnston, T., Carter, G., Merrifield, M., Pinkel, R., Worcester, P., & Dushaw, B. (2010). Interference pattern and propagation of the m2 internal tide south of the Hawaiian ridge. *Journal of Physical Oceanography*, *40*, 311–325. <https://doi.org/10.1175/2009jpo4256.1>
- Ramos-Musalem, K., & Allen, S. (2019). The impact of locally enhanced vertical diffusivity on the cross-shelf transport of tracers induced by a submarine canyon. *Journal of Physical Oceanography*, *49*, 561–584. <https://doi.org/10.1175/jpo-d-18-0174.1>
- Ray, R., & Zaron, E. (2016). Bottom pressure tides along a line in the southeast Atlantic ocean and comparisons with satellite altimetry. *Ocean Dynamics*, *46*, 3–22. <https://doi.org/10.1175/jpo-d-15-0065.1>
- Shriver, J., Arbic, B., Richman, J., Ray, R., Metzger, E., Wallcraft, A., & Timko, P. (2012). An evaluation of the barotropic and internal tides in a high-resolution global ocean circulation model. *Journal of Geophysical Research: Oceans*, *117*. <https://doi.org/10.1029/2012JC008170>
- Vic, C., Naveira Garabato, A., Green, J., Waterhouse, A., Zhao, Z., Melet, A., & Stephenson, G. (2019). Deep-ocean mixing driven by small-scale internal tides. *Nature Communication*, *10*. <https://doi.org/10.1038/s41467-019-10149-5>
- Wain, D., Gregg, M., Alford, M., Lien, R.-C., Hall, R., & Carter, G. (2013). Propagation and dissipation of the internal tide in upper Monterey canyon. *Journal of Geophysical Research: Oceans*, *118*, 4855–4877. <https://doi.org/10.1002/jgrc.20368>
- Waterhouse, A., MacKinnon, J., Musgrave, R., Kelly, S., Pickering, A., & Nash, J. (2017). Internal tide convergence and mixing in a submarine canyon. *Journal of Physical Oceanography*, *47*, 303–322. <https://doi.org/10.1175/jpo-d-16-0073.1>
- Waterhouse, A., MacKinnon, J., Nash, J., Alford, M., Kunze, E., Simmons, H., & Lee, C. (2014). Global patterns of diapycnal mixing from measurements of turbulent dissipation rate. *Journal of Physical Oceanography*, *44*, 1854–1872. <https://doi.org/10.1175/jpo-d-13-0104.1>

- Whalen, C., Talley, L., & MacKinnon, J. (2012). Spatial and temporal variability of global ocean mixing inferred from argo profiles. *Geophysical Research Letters*, 39. <https://doi.org/10.1029/2012GL053196>
- Wunsch, C., & Ferrari, R. (2004). Vertical mixing, energy and the general circulation of the oceans. *Annual Review of Fluid Mechanics*, 36, 281–314. <https://doi.org/10.1146/annurev.fluid.36.050802.122121>
- Xu, J., & Noble, M. (2009). Currents in Monterey submarine canyon. *Journal of Geophysical Research*, 114(C3). <https://doi.org/10.1029/2008jc004992>
- Yi, Y., Legg, S., & Nazarian, R. (2017). The impact of topographic steepness on tidal dissipation at bumpy topography. *Fluids*, 2, 55. <https://doi.org/10.3390/fluids2040055>
- Zaron, E., & Egbert, G. (2014). Time-variable refraction of the internal tide at the Hawaiian ridge. *Journal of Physical Oceanography*, 44, 538–557. <https://doi.org/10.1175/jpo-d-12-0238.1>
- Zhao, Z., Alford, M., Girton, J., Johnston, T., & Carter, G. (2011). Internal tides around the Hawaiian ridge estimated from multisatellite altimetry. *Journal of Geophysical Research*, 116. <https://doi.org/10.1029/2011jc007045>
- Zhao, Z., Alford, M., Girton, J., Rainville, L., & Simmons, H. (2016). Global observations of open-ocean mode-1 m2 internal tides. *Journal of Physical Oceanography*, 46, 1657–1684. <https://doi.org/10.1175/jpo-d-15-0105.1>